This is the author's version of an article that has been published in this journal. Changes were made to this version by the publisher prior to publication.
The final version of record is available at http://dx.doi.org/10.1109/TPWRD.2016.2607205

Impact of Inertia and Effective Short Circuit Ratio on Control of Frequency in Weak Grids Interfacing LCC-HVDC and DFIG-based Wind Farms

Amirthagunaraj Yogarathinam, *Student Member, IEEE*, Jagdeep Kaur, *Student Member, IEEE*, and Nilanjan Ray Chaudhuri, *Senior Member, IEEE*

***Abstract*—Although virtually every overhead HVDC line is based on LCC technology, hardly any work has been reported on modeling and analysis of the impact of inertia and effective short circuit ratio on control of frequency in weak grids interfacing LCC-HVDC and onshore DFIG-based wind farms. This paper develops a comprehensive modeling and stability analysis framework of a weak grid that interfaces an LCC-HVDC station and a DFIG-based wind farm. To that end, a nonlinear averaged phasor model of the system is derived, which is then benchmarked against a detailed switched model. The averaged model is linearized to design a frequency controller for the LCC-HVDC rectifier station. Participation factor and eigenvalue sensitivity measures indicate that the AC system electromechanical mode and the 'HVDC PLL' mode are highly sensitive to changes in Effective DC Inertia Constant and Effective Short Circuit Ratio, respectively. Root-locus analysis in a progressively weak grid validates these results. A systematic design process of the frequency controller parameters reveals a negative interaction between the 'generator speed-HVDC PLL-frequency controller' mode and the 'DFIG-GSC controller' mode.**

***Index Terms*—Weak Grid, Averaged Model, Participation Factor, Eigenvalue Sensitivity, ESCR, HVDC, DFIG.**

List of Notations

Wind farm:

s_l	slip
L_m	mutual inductance
i_{ms}	magnetizing current
K_{vc}	droop constant in RSC voltage controller
ω_{el}	base angular electrical speed
θ_{tw}	shaft angle of twist
T_m	turbine mechanical torque input
R	turbine radius
ρ/V_w	air density/wind speed
C_{sh}/K_{sh}	drive-train damping coefficient/ shaft stiffness
H_g/H_t	generator/turbine inertia constant
i_{qs}/i_{ds}	q/d-axis stator current
ω_{r_dfg}/ω_t	generator/turbine rotor speed in p.u.
e'_{qs}/e'_{ds}	q/d-axis stator transient e.m.f.
C_{Popt}/λ_{opt}	optimum power coefficient/tip-speed ratio
R_{fg}/L_{fg}	GSC filter resistance/inductance
R_{fr}/L_{fr}	RSC filter resistance/inductance
R_r/R_s	rotor/stator resistance
L_r/L_s	rotor/stator leakage inductance
x_{rr1}, x_{rr2}	RSC current controller states
x_{g1}, x_{g2}	GSC current controller states
$i_{qg}, v_{qg}/i_{dg}, v_{dg}$	q/d-axis GSC current, voltage

HVDC:

Subscripts r and i are used for the rectifier and the inverter

B	number of bridges
R_c	equivalent commutating resistance
E_{ac}	AC-side voltage phasor magnitude
T/tap	converter transformer turns/tap ratio
I_{dr}/I_{di}	rectifier/inverter DC current
v_{dr}/v_{di}	rectifier/inverter DC voltage
α/γ	firing/extinction angle
x_{r1}/x_{i1}	state of current/extinction-angle controller
K_{pR}, K_{iR}	rectifier current controller gains
K_{pi}, K_{ii}	inverter extinction angle controller gains
K_{pf}, K_{if}	rectifier frequency controller gains

Miscellaneous:

H_{dc}	effective DC inertia constant
H_{grid}	effective inertia constant of AC grid
ω_0	synchronous frequency in p.u.
$\hat{\omega}$	estimated frequency from $PLL1$
K_{p-pll}, K_{i-pll}	PLL gains

The authors are with the School of Electrical Engineering and Computer Science, Pennsylvania State University, University Park, PA, USA (e-mail: *axy43@psu.edu, juk415@psu.edu, nuc88@engr.psu.edu*).

Financial support from NSF Grant Award 1656983 is gratefully acknowledged.

I. Introduction

THE 2008 US Department of Energy (DoE) report [1] studied 20% wind-power penetration in the US Eastern Interconnection where a majority of the wind farms (WFs) were concentrated in the Midwest region due to high wind energy potential. In the Joint Coordinated System Plan (JCSP) report [2], Line Commutated Converter (LCC)-based HVDC systems were proposed to transmit power from these WFs to the load centers in the East. The Voltage Source Converter (VSC) technology was ruled out since it suffers from lower efficiency and can not match the power rating (a few GWs) of such large WFs.

Grids, where such remote WFs are interconnected, are usually 'weak' in nature as indicated by two measures [3]: (1) low Effective Short Circuit Ratio ($ESCR$), and (2) low Effective DC Inertia Constant (H_{dc}). The $ESCR$ is defined as the ratio of the short-circuit MVA of the AC system along with HVDC filters and cap-banks to the MW rating of the HVDC link. The Effective Inertia Constant H_{dc} is defined as the ratio of the total rotational inertia of the AC system in MW-s to the MW rating of the HVDC link. Typical weak

Copyright (c) 2017 IEEE. Personal use is permitted. For any other purposes, permission must be obtained from the IEEE by emailing pubs-permissions@ieee.org.

This is the author's version of an article that has been published in this journal. Changes were made to this version by the publisher prior to publication.
The final version of record is available at http://dx.doi.org/10.1109/TPWRD.2016.2607205

grids have $ESCR$ less than 2.5 and H_{dc} less than 2.0 [4]. Development of a fundamental understanding of the impact of H_{dc} and ESCR on control of frequency in weak grids interfacing LCC-HVDC and DFIG-based WFs is the subject-matter of this paper.

A lot of work has been done on the offshore wind farms (OWFs) connected to LCC-HVDC delivery systems [5]–[14]. Li *et-al* in [5] presented the damping enhancement and mitigation of the power fluctuations of a DFIG-based OWF. Traditional vector control used for DFIGs is applied along with current control in LCC-HVDC rectifier, which raises fundamental questions. It is unclear how the authors propose to use AC voltage control instead of flux control for DFIG without any voltage support at the PCC. It is also unclear how the system without the PID controller is working since a current control in the HVDC rectifier will not be able to coordinate with the power control in DFIG. Moreover, the paper did not consider any PLL dynamics, which play an important role in such studies.

References [6]–[8] reported integration of OWFs to the onshore grid via LCC-HVDC system and the control coordination thereof. In absence of any grid support, the DFIG controls were modified to supply isolated loads as was originally proposed in [15]. However, due to stringent footprint requirements, LCC-HVDC is ruled out, and the VSC technology is preferred for OWFs. Moreover, these papers did not present any modal analysis to develop further insight into the root-cause of the dynamic behavior.

Bozhko *et-al* [9], [10] and Zhou *et-al* [11], [12] introduced a STATCOM in the offshore platform for providing voltage support at the PCC. This further increases the real-estate in the offshore platform and therefore is not practical. Moreover, these papers ignored the modeling and control of DFIGs and represented them by controllable current sources. The inverter was modeled by a constant DC voltage source in [9], [10] that rules out any study following inverter-side disturbances. On the other hand the reason behind choosing the onshore self-commutated CSC over VSC proposed in [11], [12] is also unclear.

Li *et-al* [14] developed an analytical formulation of DFIG-based OWFs operating under grid-connected mode. The contribution of this important work was to design the LCC-HVDC frequency controller, albeit with a few limitations: (a) The formulation was oversimplified as it neglected the converter commutating reactance and represented the inverter-side by a DC voltage source. (b) The more viable scenario of onshore WFs connected to weak grid was not considered. As a result, the impact of $ESCR$ and H_{dc} on the system performance was not analyzed. (c) The DFIG controller dynamics including corresponding PLL were not explicitly considered.

A few papers [16]–[19] reported research on the interconnection of DFIG-based WFs with LCC-HVDC systems for onshore applications. References [16], [17] focused on frequency support from DFIG-based WFs through LCC-HVDC link to the AC grid in the inverter-side. Reference [18] oversimplified the inverter model and represented it by a DC voltage source. Yin *et-al* in [19] considers a very strong grid in the rectifier-side with a synchronous generator connected to the terminal of the LCC-HVDC station.

A detailed literature review shows that none of the papers: (a) Considered the more viable scenario of onshore WFs connected to weak grid. As a result, the impact of $ESCR$ and H_{dc} on the system performance was not analyzed. (b) Presented a comprehensive nonlinear state-space modeling framework for such systems. (c) Attempted to benchmark such models with detailed EMT-type models, and (d) Presented a stability analysis framework that can perform root-cause analysis of dynamic performance and analyze interaction of various control loops in the system with the variation of system parameters.

In this paper, a comprehensive modeling and stability analysis framework is proposed to overcome these gaps, which reveals how $ESCR$ and H_{dc} affects the frequency control in a progressively weak system in addition to the negative interaction between the 'generator speed-HVDC PLL-frequency controller' mode and the 'DFIG-GSC Controller' mode.

The paper is organized as follows: first, the nonlinear state-space averaged phasor model of the LCC-HVDC and the DFIG-based WF with their controllers is derived and benchmarked against a detailed model in EMTDC/PSCAD [20]. Following this, the frequency dynamics in a progressively weak grid is analyzed using modal participation factor, eigenvalue-sensitivity, and root locus analysis. The regulation of frequency is improved in a very weak grid through systematic design of the HVDC frequency controller and modal interaction analysis. Finally, the performance of the controller under different operating points is presented.

II. State-Space Averaged Phasor Model of the System

In this section, the non-linear state-space averaged phasor model of a power system with a DFIG-based WF connected to an LCC-HVDC is derived in the form of the following Differential and Algebraic Equations (DAEs):

$$\begin{aligned} \dot{x} &= f(x,u,z) \\ 0 &= g(x,u,z) \end{aligned} \tag{1}$$

where x, u, and z are the state-variables, input variables, and algebraic variables, respectively. To avoid conflicts in a multi-vendor context the nonlinear state-space model of individual subsystems can be directly obtained from different vendors with access to the identity of x, u and z, and thereby, masking the need for explicitly communicating the structure of the controllers, etc. Figure 1 shows the schematic of the LCC-HVDC with its rectifier operating under current control (CC) and inverter operating under extinction angle control. Figure 2 shows the schematic of a DFIG-based WF with its components and controllers, which is connected to the rectifier station PCC. The PCC is a part of an AC grid modeled by an ideal source behind impedance Z_{grid}, as highlighted in Fig. 2.

LCC-HVDC: State-Space Averaged Model

The Rectifier and the Inverter stations are represented by their respective algebraic equations:

$$\begin{aligned} v_{dr} &= \tfrac{3\sqrt{2}BT_r tap_r E_{acr}}{\pi}\cos\alpha_r - R_{cr}I_{dr} \\ v_{di} &= \tfrac{3\sqrt{2}BT_i tap_i E_{aci}}{\pi}\cos\gamma_i - R_{ci}I_{di} \end{aligned} \tag{2}$$

The DC line is represented by a T-model, which has three dynamic states - I_{dr}, I_{di}, and V_{dm}. The capacitor banks and

Copyright (c) 2017 IEEE. Personal use is permitted. For any other purposes, permission must be obtained from the IEEE by emailing pubs-permissions@ieee.org.

This is the author's version of an article that has been published in this journal. Changes were made to this version by the publisher prior to publication.
The final version of record is available at http://dx.doi.org/10.1109/TPWRD.2016.2607205

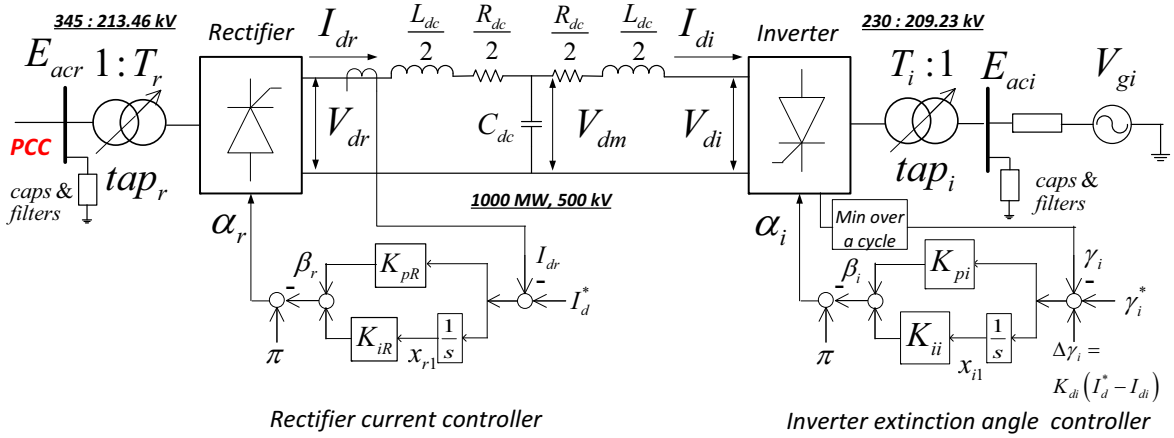

Fig. 1. Schematic of 500-kV, 1000-MW LCC-HVDC with its controllers. DFIG-based WF is connected at the PCC as shown in Fig. 2.

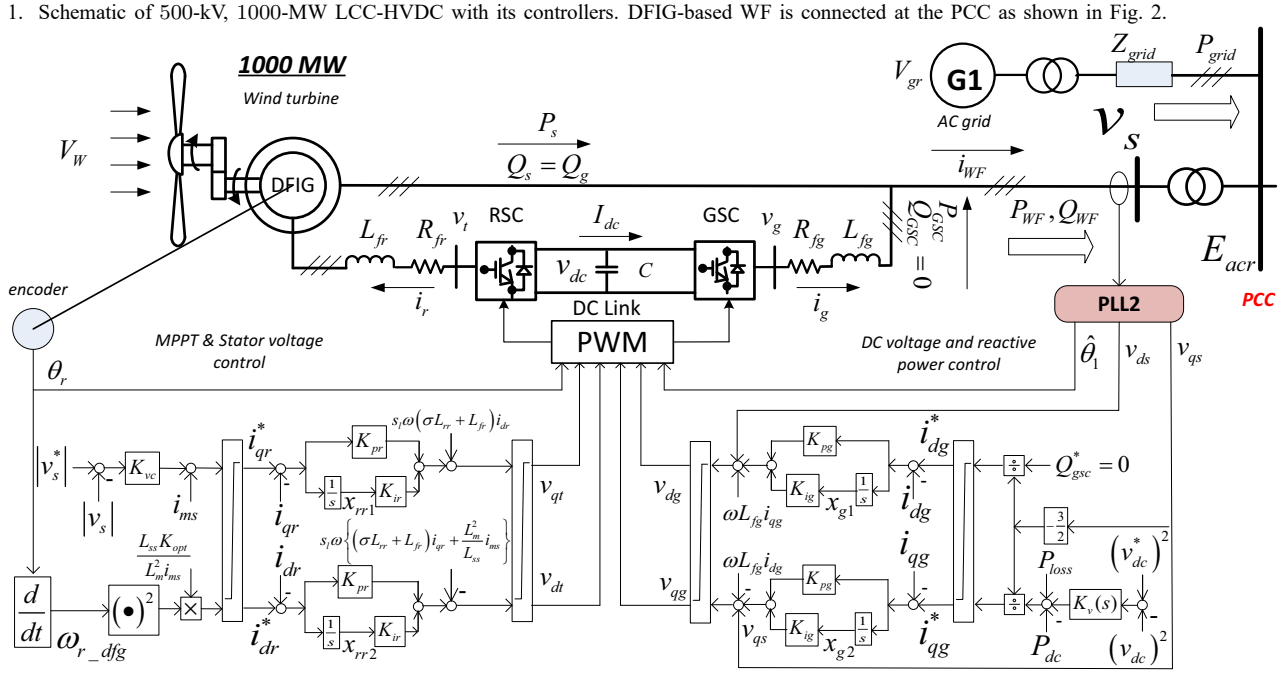

Fig. 2. Schematic of DFIG-based 1000-MW WF with its controllers. The WF is connected to an AC grid at the PCC. A 500-kV, 1000-MW LCC-HVDC rectifier station is also connected at the PCC as shown in Fig. 1.

filters at the rectifier and the inverter stations are modeled as constant impedance loads at the fundamental frequency. Rearranging the algebraic and differential equations, one can derive the nonlinear state-space averaged phasor model of the LCC-HVDC and its controllers as:

$$
\begin{aligned}
\dot{I}_{dr} &= -\left(\tfrac{R_{dc}+2R_{cr}}{L_{dc}}\right) I_{dr} - \left(\tfrac{2}{L_{dc}}\right) v_{dm} - \left(\tfrac{6\sqrt{2}}{\pi}\right) \\
&\quad \times \left(\tfrac{BT_r tap_r}{L_{dc}}\right) E_{acr} \cos\left\{K_{pR}\left(I_d^* - I_{dr}\right) + K_{iR} x_{r1}\right\} \\
\dot{x}_{r1} &= I_d^* - I_{dr} \\
\dot{I}_{di} &= -\left(\tfrac{R_{dc}}{L_{dc}}\right) I_{di} + \left(\tfrac{2}{L_{dc}}\right) v_{dm} \\
&\quad - \left(\tfrac{2}{L_{dc}}\right) \overbrace{f\left(I_{di}, x_{i1}, v_{dm}, I_d^*, \gamma_i^*, E_{aci}\right)}^{v_{di}} \\
\dot{x}_{i1} &= \gamma_i^* - \gamma_i + K_{di}\left(I_d^* - I_{di}\right) \\
\dot{v}_{dm} &= \tfrac{1}{C_{dc}}\left(I_{dr} - I_{di}\right)
\end{aligned}
\tag{3}
$$

Please note $v_{di} = f\left(I_{di}, x_{i1}, v_{dm}, I_d^*, \gamma_i^*, E_{aci}\right)$ is obtained by substituting the following expression in equation (2).

$$
\begin{aligned}
&\gamma_i - \tfrac{1}{K_{pi}} \cos^{-1}\left(-\cos\gamma_i + \tfrac{6X_{ci}\pi}{3\sqrt{2}T_i tap_i E_{aci}} I_{di}\right) \\
&= -\tfrac{\pi}{K_{pi}} + \gamma_i^* + K_{di}\left(I_d^* - I_{di}\right) + \left(\tfrac{K_{ii}}{K_{pi}}\right) x_{i1}
\end{aligned}
\tag{4}
$$

The state-variables x, input variables u, and the algebraic variables z in the LCC-HVDC model are:

$$
x = \begin{bmatrix} I_{dr} & x_{r1} & I_{di} & x_{i1} & v_{dm} \end{bmatrix}^T,
$$
$$
u = \begin{bmatrix} I_d^* & \gamma_i^* \end{bmatrix}^T, z = \begin{bmatrix} E_{acr} & E_{aci} \end{bmatrix}^T
$$

DFIG-based WF: State-Space Averaged Model

The WF is represented by an aggregated model (Fig. 2) whose turbine-generator rotational dynamics is represented by a two-mass model. The blade pitch angle is assumed to be constant, which will be relaxed in Section VII. The DFIG model including the controls is derived based on a synchronous $d-q$ reference frame, rotating at a p.u. angular frequency ω, which is equal to the system frequency, and varies under dynamical conditions. The d-axis is assumed to lead the q-axis. The following points are worth noting:

☐ Stator transients of the induction machine are neglected.

☐ The tie-reactors of the VSCs, DC-link dynamics, and the PLL dynamics are included in the model (Fig. 2).

☐ Standard vector control approach was considered for both rotor-side converter (RSC) and the grid-side converter (GSC) controls, as mentioned in [21]. For Maximum Power Point Tracking (MPPT) and stator terminal voltage control for the

Copyright (c) 2017 IEEE. Personal use is permitted. For any other purposes, permission must be obtained from the IEEE by emailing pubs-permissions@ieee.org.

This is the author's version of an article that has been published in this journal. Changes were made to this version by the publisher prior to publication.
The final version of record is available at http://dx.doi.org/10.1109/TPWRD.2016.2607205

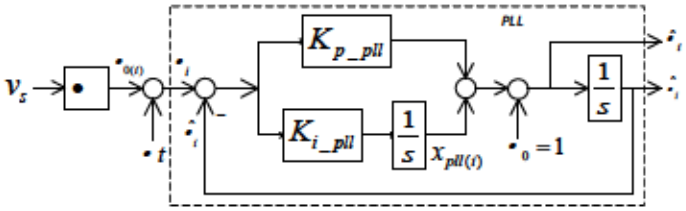

Fig. 3. Model for the i^{th} Phase-lock-loop (PLL) [22].

RSC (see Fig. 2), the stator flux is aligned with the q-axis. For DC voltage control and reactive power control of the GSC (see Fig. 2), the stator terminal voltage vector is aligned with the q-axis.

□ Due to space restrictions, only the final state-space model is presented in a compact form in Appendix I.

□ The PLL model [22] is shown in Fig. 3. This model was used for $PLL2$ shown in Fig. 2. The state-equations are described in equation (5).

$$\begin{aligned} \dot{\hat{\theta}}_i &= -K_{p\_pll}\hat{\theta}_i + x_{pll(i)} + K_{p\_pll}\theta_i + \omega_0 \\ \dot{x}_{pll(i)} &= -K_{i\_pll}\hat{\theta}_i + K_{i\_pll}\theta_i \end{aligned} \tag{5}$$

The state-variables x, input variables u, and the algebraic variables z in the DFIG-based WF model are:

$$x = [\ \omega_{r\_dfg}\ \ \omega_t\ \ \theta_{tw}\ \ i_{qs}\ \ i_{ds}\ \ e'_{qs}\ \ e'_{ds}\ \ i_{ms}\ \ v_{dc}^2 \cdots \ i_{qg}\ \ i_{dg}\ \ x_{rr1}\ \ x_{rr2}\ \ x_{g1}\ \ x_{g2}\ \ \hat{\theta}_2\ \ x_{pll(2)}\ \ i^*_{qg}\ \ x_v]^T$$

$$u = [\ V_w\ \ |v^*_s|\ \ (v^*_{dc})^2\ \ Q^*_{gsc}\ \ \theta_t\ ]^T,\ \ z = [\ |v_s|\ \ v_{qs}]^T$$

Here, i^*_{qg}, and x_v are the state-variables of the DC-link voltage controller with gain K_{dc}, which was not described in the model due to space restrictions.

AC Network Model

The AC network is modeled algebraically using a Y-bus matrix. The set of algebraic equations

$$0 = [I] - [Y_{bus}][V_{bus}] \tag{6}$$

is solved at each solution time-step. It takes the current injection vector $[I]$ from HVDC, WF, AC source, and the capacitors and filter banks as the input, and generates node voltage vector $[V_{bus}]$ as output. To build confidence in the accuracy of the model, its performance is benchmarked against a detailed model built in EMTDC/PSCAD, as described next.

III. Benchmarking with Detailed Model

The state-space averaged model developed in the previous section was benchmarked against a detailed three-phase model in EMTDC/PSCAD that considers converter switching. As mentioned before, the AC grid connected to the PCC (see Figs. 1 and 2) in this simulation was modeled using an ideal source behind an impedance. The accuracy of the state-space averaged model has been validated with the following dynamic response of the system:

Case 1: The response of the system after a step-reduction in the current reference of the rectifier current controller which excites the LCC-HVDC dynamics is shown in Fig. 4.

Case 2: Fig. 5 shows the system response after a step-reduction in the wind speed, which excites the WF dynamics.

Case 3: In this case a pulse change in rectifier-side grid voltage is applied and the system response can be seen in Fig. 6.

All the responses from the averaged model and the detailed model match closely, and thus validates the accuracy of the state-space averaged model.

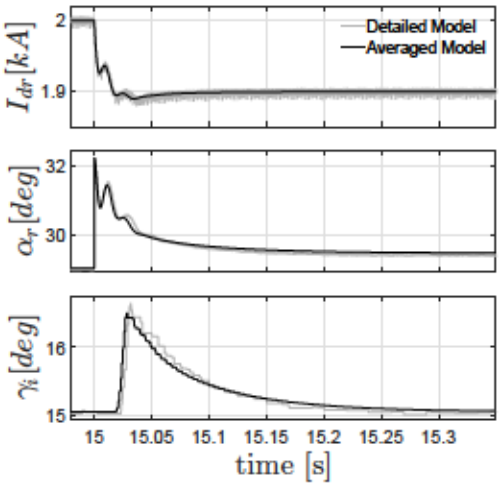

Fig. 4. Dynamic response of the system following a step-reduction in the current reference of the rectifier current controller. Response in γ_i is delayed by a cycle following the disturbance due to the minimum-over-a-cycle measurement of γ_i in the feedback signal, see Fig. 1.

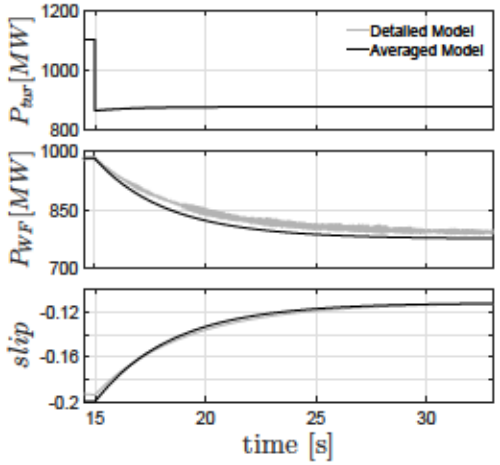

Fig. 5. Dynamic response of the system following a step-reduction in wind speed (V_w).

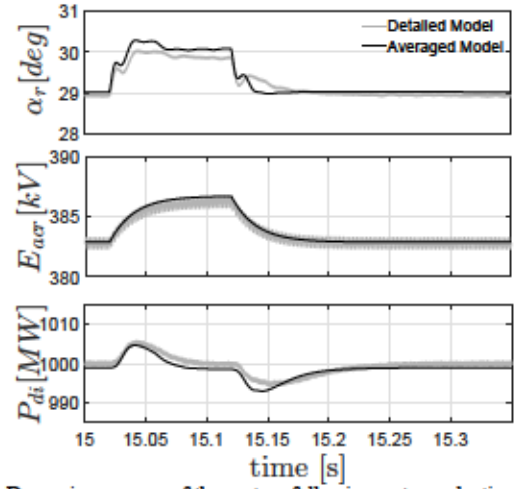

Fig. 6. Dynamic response of the system following a step-reduction in rectifier side grid voltage (V_{gr}).

Copyright (c) 2017 IEEE. Personal use is permitted. For any other purposes, permission must be obtained from the IEEE by emailing pubs-permissions@ieee.org.

This is the author's version of an article that has been published in this journal. Changes were made to this version by the publisher prior to publication.
The final version of record is available at http://dx.doi.org/10.1109/TPWRD.2016.2607205

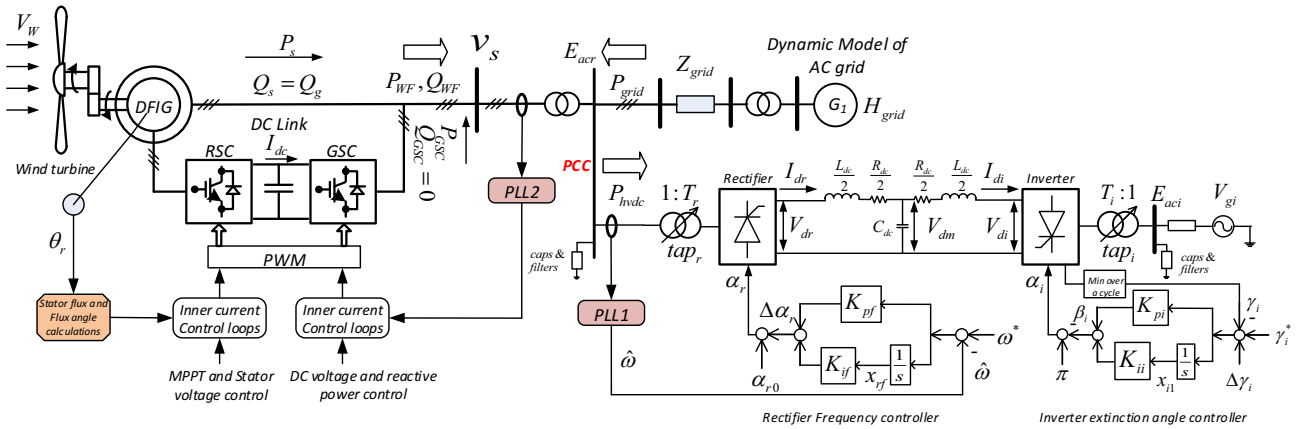

Fig. 7. Schematic of DFIG-based WF connected to LCC-HVDC in an AC grid represented by a dynamic model. Values of Z_{grid} can be gradually increased and H_{grid} can be reduced to simulate a progressively weak AC system. The HVDC rectifier station operates in a constant frequency control mode.

IV. Dynamic Model Representing Weak AC System: LCC-HVDC Frequency Controller

After gaining confidence in the accuracy of the averaged model, the rectifier-side AC source in Fig. 2 is replaced by a dynamic model to simulate a weak AC grid with low ESCR and H_{dc}.

Dynamic Model Representing Weak AC System

Figure 7 shows the schematic of the AC system connected at the PCC of the DFIG-based WF and the LCC-HVDC. The synchronous generator G_1 is represented by a sixth-order subtransient model, where the stator transient was neglected. An IEEE $DC1A$ type excitation system and a turbine-governor is also considered for the generator. The state-space representation of generators, governors, and exciters can be found in standard texts like [3], and is not repeated here.

Frequency Control in LCC-HVDC

It is proposed that, the LCC-HVDC rectifier station operates under a constant frequency control mode as in [14], which is shown in Fig. 7 while the inverter-side control is the same as discussed in Section II. The rectifier side Frequency controller facilitates two important objectives:

- Ensures stability in the frequency dynamics, provided the frequency controller is designed appropriately, and
- Ensures that the power generated by the WF (P_{WF}) and the AC grid (P_{grid}) flow through the HVDC rectifier to the AC system on the inverter-side.
- Ensures stable operation of the PLL in strong AC grid scenario as well (discussed in Section VII).

The frequency is estimated at the rectifier bus using $PLL1$, which has the same structure shown in Fig. 3. Usually, the rectifier PLL is also used to calculate the zero crossing points of the voltage waveform and thus generate the firing pulses from the firing angle command. The nonlinear averaged phasor model developed in this paper cannot consider such zero-crossing points of the voltage waveform. A PI compensator is used to generate the firing angle α_r for the rectifier to maintain constant frequency.

Due to the introduction of frequency controller, the state-space model of the LCC-HVDC described in equation (3) requires modification by replacing the state-variable x_{r1} with a new state-variable x_{rf} shown in Fig. 7. The state equation for I_{dr} will also be modified as shown in equation (7).

$$\begin{aligned}\dot{x}_{rf} &= \omega^* - \hat{\omega} \\ \dot{I}_{dr} &= -\left(\tfrac{R_{dc}+2R_{cr}}{L_{dc}}\right) I_{dr} - \left(\tfrac{2}{L_{dc}}\right) v_{dm} + \left(\tfrac{6\sqrt{2}}{\pi}\right)\left(\tfrac{1}{L_{dc}}\right) \\ &\times (BT_r tap_r)\, E_{acr} \cos\left\{\alpha_{r0} + K_{pf}\left(\omega^* - \hat{\omega}\right) + K_{if} x_{rf}\right\}\end{aligned} \tag{7}$$

V. Analysis of Frequency Dynamics in a Progressively Weak System

The objective of this section is to develop a deeper understanding of the frequency dynamics of the system shown in Fig. 7 through modal analysis when the system is made progressively weaker by decreasing H_{dc} and $ESCR$ of the AC grid with reduction of H_{grid} and increase of Z_{grid}, respectively.

The AC system frequency f is determined by the angular speed ω of the synchronous generator G_1. A power-balance equation at the PCC, neglecting losses, leads to $P_{WF}+P_{grid} = P_{hvdc}$. With the q-axis aligned to the stator flux and with an approximation $E_{acr} \approx v'_{ds} \approx L_m i_{ms}\omega$ [14], one can write:

$$\begin{aligned}\tfrac{d\omega}{dt} &= \tfrac{3L_m i_{ms}}{2H_{grid}}\left\{-\tfrac{\sqrt{2}}{\pi}\left(BT_r tap_r I_{dr}\cos\alpha_r\right) + \tfrac{1}{2} i'_{dWF}\right\}\omega \\ &+ \tfrac{1}{2H_{grid}}\left\{\tfrac{3}{2} v'_{qs} i'_{qWF} + P_{mgrid} + \tfrac{3}{\pi} X_{cr} B I_{dr}^2 + \tfrac{(1-\omega)}{R_{gov}}\right\}\end{aligned} \tag{8}$$

where, P_{mgrid} is the mechanical power input to G_1, R_{gov} is the governor droop coefficient, i'_{qWF}/i'_{dWF} are q/d-axis components of total WF current i_{WF} with the q-axis aligned to the stator flux. It is clear that the dynamics in ω is influenced by the dynamics of LCC-HVDC, WF, synchronous generator and their respective controllers, including the PLLs. Please note that this approximate expression is used just for qualitative understanding. The analysis that follows does not use such an approximation.

To perform modal analysis, the state-space averaged model developed in Sections II and IV, which was expressed in a compact form in equation (1), is linearized around an operating point (x_0, u_0, z_0), see Appendix II, and expressed in state-space form as:

$$\Delta\dot{x} = A\Delta x + B\Delta u + \tau\Delta z \tag{9}$$

where, Δx and A are the state-vector and the state-matrix, respectively. The right (ϕ_i) and the left (ψ_i) eigen vectors corresponding to the eigenvalues λ_i , $i = 1, 2, ..., n$ satisfy:

$$A\phi_i = \lambda_i\phi_i,\ \ \psi_i A = \lambda_i\psi_i \tag{10}$$

The k^{th} element of the right eigenvector ϕ_i measures the activity of the state variable Δx_k in the i^{th} mode while that of

Copyright (c) 2017 IEEE. Personal use is permitted. For any other purposes, permission must be obtained from the IEEE by emailing pubs-permissions@ieee.org.

This is the author's version of an article that has been published in this journal. Changes were made to this version by the publisher prior to publication.
The final version of record is available at http://dx.doi.org/10.1109/TPWRD.2016.2607205

TABLE I
MODAL PARTICIPATION & EIGENVALUE SENSITIVITY ANALYSIS FOR STRONG SYSTEM: NOMINAL $H_{dc} = 5.85s$, $ESCR = 4.37$, $K_{pf} = 0.754$, $K_{if} = 7.54$, $\Delta\Gamma < 0$, I.E. PARAMETERS WERE REDUCED

Dominant States	Modes $\lambda_i = \sigma_i \pm j\omega_{di}$	$\frac{\partial\sigma_i}{\partial\Gamma}$		$\frac{\partial\omega_{di}}{\partial\Gamma}$	
		H_{dc}	$ESCR$	H_{dc}	$ESCR$
$G1:\ \boldsymbol{\omega}$, $PLL1: \hat{\boldsymbol{\theta}}_{\mathbf{1}}$, $Freq\ Controller: \boldsymbol{x_{rf}}$	$-0.20 \pm j0.98$	0.18	0.01	-0.64	0.02
$PLL1: \hat{\boldsymbol{\theta}}_{\mathbf{1}}$	$-273.47 \pm j605.28$	0.12	-84.80	-0.17	-61.44
$PLL1: \hat{\boldsymbol{x}}_{\boldsymbol{pll(1)}}$	$-527.40 \pm j531.44$	0.00	2.85	0.00	-0.01
$PLL2: \hat{\boldsymbol{x}}_{\boldsymbol{pll(2)}}$	$-533.10 \pm j533.24$	0.00	-0.00	0.00	-0.00
$GSC: \boldsymbol{i_{qg}}, \boldsymbol{x_{g1}}$	$-516.01 \pm j1357.78$	-0.11	72.51	-0.15	-490.69

the left eigenvector ψ_i weighs the contribution of this activity to the i^{th} mode [3].

For modal analysis of frequency dynamics in the progressively weak AC system, a three-step approach is proposed:

□ **Step I: Modal participation analysis** was performed to figure out the nature and the root cause of the dynamic response of frequency in a strong AC grid. It should be mentioned that the participation matrix, P whose elements $p_{ki} = \phi_{ki}\psi_{ik}$ are termed as the participation factor.

Attention was paid to identify the modes with high participation from the dynamic state ω and the dynamic state x_{rf} of the frequency controller. Since the frequency controller works based on the frequency $\hat{\omega}$, estimated by $PLL1$, it is important to identify the modes with high participation from the states of $PLL1$. Similarly, dynamic states of $PLL2$ should also be considered in this study.

□ **Step II: Eigenvalue-sensitivity analysis** with respect to H_{dc} and $ESCR$ of the AC system was performed to evaluate how the above-mentioned modes are impacted by a progressively weak system. Eigenvalue sensitivity is considered as a very important measure in the area of small signal stability, and has been used in various applications in the past. The 1^{st}-order eigenvalue sensitivity is given by [23]:

$$\boxed{\frac{\partial\lambda_i}{\partial\Gamma} = \frac{\psi_i \frac{\partial A}{\partial\Gamma}\phi_i}{\psi_i\phi_i}} \tag{11}$$

where, Γ is a system parameter. The sensitivity was approximated by $\frac{\psi_i \frac{\Delta A}{\Delta\Gamma}\phi_i}{\psi_i\phi_i}$ where ΔA denotes the change in the state-matrix corresponding to a small change in parameter Γ.

□ **Step III: Root locus analysis** was performed to observe the eigenvalue movement as the system is made progressively weaker by gradual reduction in H_{dc} and $ESCR$.

A. Results & Analysis

For the test system shown in Fig. 7, Steps I and II were performed assuming a strong nominal system with $H_{dc} = 5.85s$ and $ESCR = 4.37$. The following are the key observations from Table I, which summarizes these results:

- The eigenvalue-sensitivity was computed by reducing the parameters H_{dc} and $ESCR$. Therefore, apositive $\frac{\partial\sigma_i}{\partial\Gamma}$ indicates eigenvalue moving towards left and a positive $\frac{\partial\omega_{di}}{\partial\Gamma}$ indicates a reduction of the value ω_{di}.
- The states ω, $\hat{\theta}_1$, and x_{rf} participate primarily in a low frequency mode $-0.20 \pm j0.98$. As observed from equation (8), H_{grid}, and therefore, H_{dc} has direct impact on this mode. This is verified from the eigen-sensitivity values shown in Table I. When H_{dc} is reduced, the real part becomes slightly more negative and the imaginary part increases significantly. This eigenvalue has a negligible sensitivity w.r.t. the $ESCR$.
- The mode $-273.47 \pm j605.28$ that is dominated by the dynamic-state $\hat{\theta}_1$ of $PLL1$, is highly sensitive to change in $ESCR$ and moves towards right with an increase in frequency when $ESCR$ is reduced. Therefore stability of such PLL-modes sould be evaluated for weak systems.
- The states x_{pll1} and x_{pll2} of $PLL1$ and $PLL2$ participate in one pair of pole each, which are very close to each other and are insensitive to the changes in system strength.

In Step III, the values of H_{grid} and $ESCR$ are reduced to analyze a progressively weaker system. Figure 8 shows the movement of the eigenvalues of interest. Figure 8(a) highlights the movement of the mode $-0.20 \pm j0.98$ with reduction in H_{dc} from $5.85s$ to $1.35s$ while $ESCR$ remains unchanged at 4.37. As shown in Fig. 8(b), the eigenvalue $-273.47 \pm j605.28$ moves towards right and its frequency increases when $ESCR$ reduces to 0.17. There is another mode $-516.01 \pm j1357.78$ that moves a lot towards left and then turns back towards right at very low $ESCR$. Participation factor analysis confirms that this is a WF GSC mode, which is shown in Table I.

Finally, both H_{dc} and $ESCR$ were reduced simultaneously to 1.35 and 0.17, respectively, which makes the system very weak. The loci of the eigenvalues corresponding to this change is shown in Figs 8(c) and (d). It should be noted that these movements are all in line with the expectations from Table I.

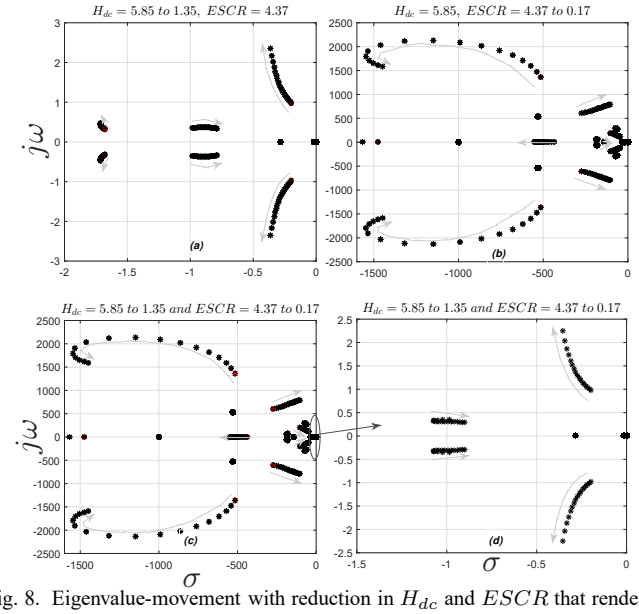

Fig. 8. Eigenvalue-movement with reduction in H_{dc} and $ESCR$ that renders the system progressively weaker. (a) only H_{dc} is reduced from $5.85s$ to $1.35s$ while $ESCR$ remains unchanged at 4.37. (b) only $ESCR$ is reduced from 4.37 to 0.17 while H_{dc} remains unchanged at $5.85s$. (c) H_{dc} is reduced from $5.85s$ to $1.35s$ and $ESCR$ is reduced from 4.37 to 0.17 simultaneously. (d) zoomed view of subplot (c).

VI. IMPROVING CONTROL OF FREQUENCY IN A VERY WEAK SYSTEM

The system shown in Fig. 7 with $H_{dc} = 1.35s$ and $ESCR = 0.17$ can be considered a very weak AC system.

Copyright (c) 2017 IEEE. Personal use is permitted. For any other purposes, permission must be obtained from the IEEE by emailing pubs-permissions@ieee.org.

This is the author's version of an article that has been published in this journal. Changes were made to this version by the publisher prior to publication.
The final version of record is available at http://dx.doi.org/10.1109/TPWRD.2016.2607205

TABLE II
MODAL PARTICIPATION & EIGENVALUE SENSITIVITY ANALYSIS FOR A VERY WEAK SYSTEM: NOMINAL $H_{dc} = 1.35s$, $ESCR = 0.17$, $K_{pf} = 0.754$, $K_{if} = 7.54$, $\Delta\Gamma < 0$, I.E. PARAMETERS WERE REDUCED

Dominant States	Modes $\lambda_i = \sigma_i \pm j\omega_d$	$\frac{\partial\sigma_i}{\partial\Gamma}$				$\frac{\partial\omega_{di}}{\partial\Gamma}$			
		K_{pf}	K_{if}	K_{p_pll}	K_{dc}	K_{pf}	K_{if}	K_{p_pll}	K_{dc}
$\boldsymbol{\omega, \hat{\theta}_1, x_{rf}}$	$-0.35 \pm j2.27$	-0.18	0.22	0.00	0.00	0.02	0.75	0.0	0.00
$\boldsymbol{i_{qs}, i_{qg}, e'_{ds}, \hat{\theta}_1, x_{g1}}$	$-105.41 \pm j793.58$	122.65	-2.06	38.05	-32.15	-150.36	-1.27	153.30	244.27

The control of the frequency of this weak AC system is improved considering the design of appropriate controller parameters. To that end the following systematic procedure is adopted:

Step A: Determine critical modes impacted by H_{dc} & $ESCR$

Two such modes are $-0.20 \pm j0.98$ and $-273.47 \pm j605.28$, which moved to $-0.35 \pm j2.27$ and $-105.41 \pm j793.58$, respectively, following the reduction in H_{dc} to $1.35s$ and $ESCR$ to 0.17, see Figs 8(c) and 8(d).

Step B: Determine dominant participating states in those modes

Modal participation factor analysis was performed on all the states of the system and the dominant participating states in the modes of interest from step A are listed in Table II. It can be seen that dominant states in the poorly-damped mode are from $G1: \omega$, $PLL1: \hat{\theta}_1$, Freq Controller: x_{rf}. The dominant states participating in the other mode is a combination of states from DFIG, GSC, GSC current controller, and PLL1.

Step C: Select candidate controllers using eigenvalue sensitivity

Eigenvalue-sensitivity analysis with respect to different controller parameters was performed for these modes of interest, which are shown in Table II. Sensitivities with significant order of magnitudes are highlighted.

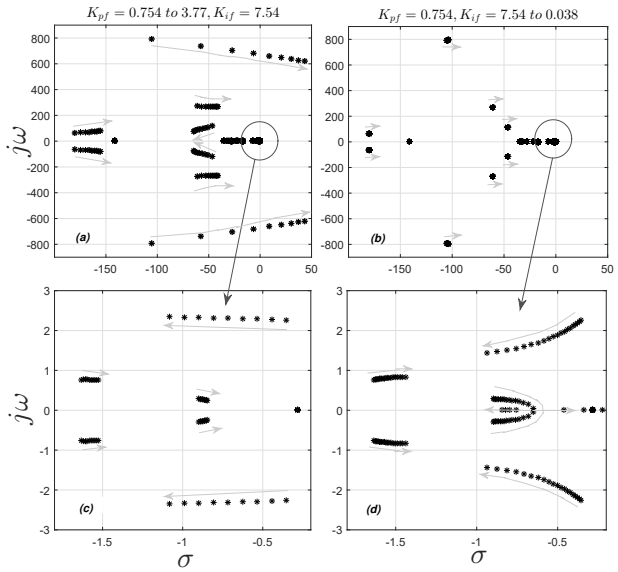

Fig. 9. Movement of eigenvalues with: (a), (c) increase in K_{pf}, and (b), (d) decrease in K_{if}.

The following are the key observations:

- It can be seen that the real-part of poorly-damped $0.36Hz$ mode has high sensitivity w.r.t. K_{pf} and K_{if}. Increasing K_{pf} and decreasing K_{if} will improve the damping of this mode. A closer look at the values corresponding to the imaginary part reveals that a decrease in K_{if} decreases the modal frequency, whereas such a change is insignificant when K_{pf} is changed.
- Parameters K_{pf} and K_{if} appear to be the the best choice for improving frequency dynamics in the system. However, sensitivity of the other eigenvalue $-105.41 \pm j793.58$ with dominant participation from $i_{qs}, i_{qg}, e'_{ds}, \hat{\theta}_1, x_{g1}$ reveals negative interaction with the mode $-0.35 \pm j2.27$ that has a dominant participation from ω, $\hat{\theta}_1$, x_{rf}. This is clear from the opposite signs of the sensitivities, e.g. -0.18 vs 122.65 for K_{pf} and 0.22 vs -2.06 for K_{if}.

Step D: Design frequency controller using root-locus method

The controller parameters K_{pf} and K_{if} are designed using root-locus method while utilizing the eigenvalue sensitivity information from Step C. The following steps are followed:

- The value of K_{pf} was increased by 5-times while keeping K_{if} constant at 7.54. As shown in Fig. 9(c), this improves the damping of the $-0.35 \pm j2.27$ mode with insignificant change in modal frequency. However, Fig. 9(a) shows that the mode $-105.41 \pm j793.58$ crosses into the right-half of s-plane.
- Figure 9(d) shows that a decreasing K_{if} to 0.038 while keeping K_{pf} constant at 0.754 moves the dominant pole $-0.35 \pm j2.27$ towards the left and also decreases its frequency, which is in agreement with the eigenvalue sensitivity figures mentioned in Table II. It is also verified from Fig. 9(b) that this change has hardly any impact on the movement of other poles. Thus $K_{pf} = 0.754$ and $K_{if} = 0.038$ are chosen as the designed values.

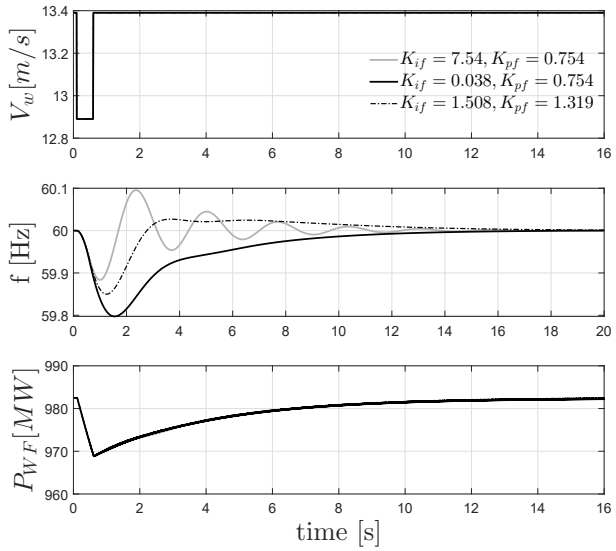

Fig. 10. Dynamic response of the system following a pulse-change in wind speed. Grey trace: response with $K_{if} = 7.54$, $K_{pf} = 0.754$. Black trace: $K_{if} = 0.038s$, $K_{pf} = 0.754$. Dotted trace: $K_{if} = 1.508$, $K_{pf} = 1.319$.

The performance of the frequency controller is compared against the response with the nominal values, i.e. $K_{pf} = 0.754$ and $K_{if} = 7.54$. The time-domain simulations were performed using the nonlinear averaged phasor model which was presented in Sections II and IV. A pulse-change in the wind-speed V_w is created in the test system shown in Fig. 7. Even

Copyright (c) 2017 IEEE. Personal use is permitted. For any other purposes, permission must be obtained from the IEEE by emailing pubs-permissions@ieee.org.

This is the author's version of an article that has been published in this journal. Changes were made to this version by the publisher prior to publication.
The final version of record is available at http://dx.doi.org/10.1109/TPWRD.2016.2607205

though a wind pulse is unrealistic, it is nevertheless useful to study how pole position affects overall system dynamics. The dynamic performance of the system following this disturbance is shown in Figs 10 and 11. With a reduction in V_w, the WF power output P_{WF} drops and as the wind velocity increases, it comes back to pre-disturbance value. No oscillation is observed in P_{WF} since the RSC controls the DFIG speed very tightly to ensure MPPT.

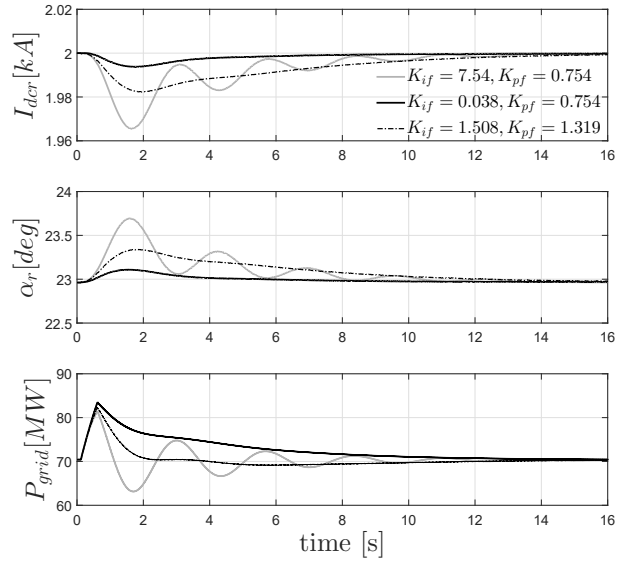

Fig. 11. Dynamic response of the system following a pulse-change in wind speed. Grey trace: response with $K_{if} = 7.54$, $K_{pf} = 0.754$. Black trace: $K_{if} = 0.038$, $K_{pf} = 0.754$. Dotted trace: $K_{if} = 1.508$, $K_{pf} = 1.319$.

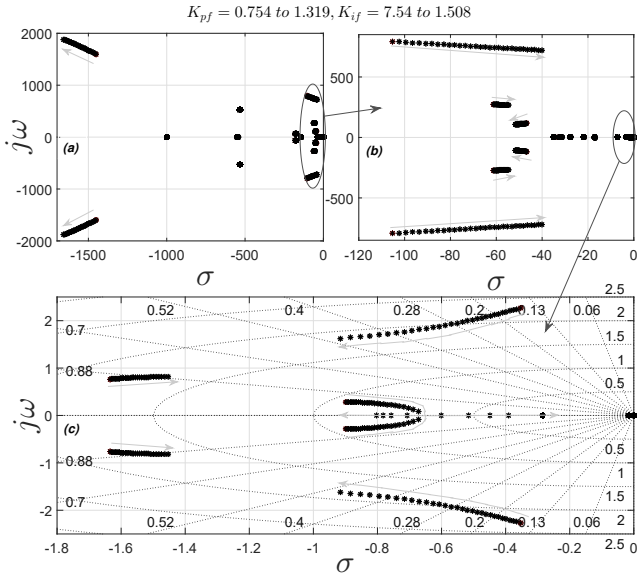

Fig. 12. Movement of eigenvalues with (a) increase in K_{pf} to 1.319 and simultaneous decrease in K_{if} to 1.508; (b), (c) zoomed view of (a).

Responses denoted in grey trace correspond to the case with $K_{if} = 7.54$, $K_{pf} = 0.754$, where the $0.36Hz$-mode

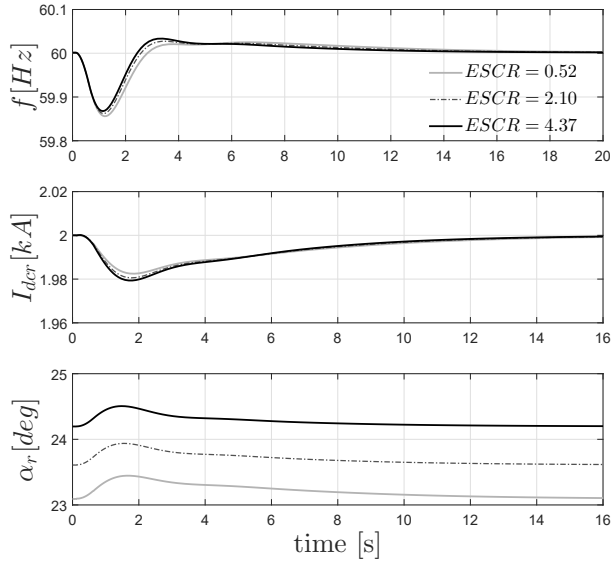

Fig. 13. Dynamic response of the system after pulse change in wind speed with different $ESCR$ values. Grey trace: response with $ESCR = 0.52$; dotted trace:$ESCR = 2.10$; Black trace:$ESCR = 4.37$.

is clearly visible in the frequency of the system since the generator speed ω has the highest participation in that mode (Fig. 10). The same mode is observable in the oscillations of I_{dcr}, α_r, and P_{grid} (Fig. 11). Following the design procedure mentioned before, the values of K_{if} and K_{pf} are set to 0.038 and 0.754, respectively, which improves the damping of the concerned mode from 15% to 58%. The dynamic response with this design are shown with black traces in Figs 10 and 11, which confirms a much better damping. It can be observed from Fig. 10 that this design leads to a larger dip in frequency ($59.8Hz$) compared with the case with poorer damping.

To address this issue, the value of K_{pf} was increased and K_{if} decreased simultaneously. Figure 12 shows the eigenvalue movement when K_{pf} was increased from 0.754 to 1.319, and K_{if} is reduced from 7.54 to 1.508. As shown in Fig. 12(b), this ensures that the $-105.41 \pm j793.58$ mode does not become unstable while a 50% damping-ratio is achieved for the poorly-damped mode, see Fig. 12(c). The dotted traces in Figs 10 and 11 show the dynamic performance with this design following a pulse disturbance in the wind speed. Improvement in the frequency-dip is clearly visible from the the nonlinear time-domain simulation.

VII. Performance across Operating Points: Inclusion of Pitch Controller

To further exploit the capability of the proposed framework the pitch angle controller is also included in the DFIG-based WF. The performance of the proposed controller is evaluated under different operating points by varying the ESCR and the wind speed.

■ **Different ESCR scenarios:** Figure 13 shows the system

TABLE III
Variation of Modes of Interest with Different Operating Points: Nominal $H_{dc} = 1.35s$, $ESCR = 0.52$, $K_{pf} = 1.319$, $K_{if} = 1.508$

Dominant States	Modes				
	$V_w = 12.4\ m/s$	$V_w = 12.8\ m/s$	$V_w = 13.2\ m/s$	$V_w = 13.8\ m/s$	$V_w = 14.3\ m/s$
$\boldsymbol{\omega, \hat{\theta}_1, x_{rf}}$	$-0.997 \pm j1.673$	$-1.009 \pm j1.683$	$-1.002 \pm j1.646$	$-0.972 \pm j1.594$	$-0.949 \pm j1.565$
$\boldsymbol{i_{qs}, i_{qg}, e'_{ds}, \hat{\theta}_1, x_{g1}}$	$-75.28 \pm j620.0$	$-66.88 \pm j649.0$	$-59.07 \pm j679.0$	$-51.94 \pm j710.0$	$-45.640 \pm j742.4$

Copyright (c) 2017 IEEE. Personal use is permitted. For any other purposes, permission must be obtained from the IEEE by emailing pubs-permissions@ieee.org.

This is the author's version of an article that has been published in this journal. Changes were made to this version by the publisher prior to publication.
The final version of record is available at http://dx.doi.org/10.1109/TPWRD.2016.2607205

response following a pulse disturbance in V_w with increasing $ESCR$. The response of frequency and I_{dcr} is similar to the previous case (Figs 10 and 11) when pitch controller was not included.

■ **Different wind speed conditions:** When the wind speed is varied the corresponding modes of interest are listed in Table III. It reveals that all the modes are stable without much deviation in the damping ratio of the critical low frequency mode. To validate the findings of frequency-domain analysis the following time-domain simulations have been carried out:

Inverter-side disturbance: The dynamic response of the system after a large disturbance on the inverter side grid voltage (V_{gi}) leading to overfrequency scenario at different wind speeds is shown in Fig. 14.

Performance under fault: When a three-phase high impedance self-clearing fault occurs at the rectifier side AC system, the system response under different wind speeds can be seen in Fig. 15.

The analysis further validates the robustness of the frequency controller for different operating conditions and disturbances in the system.

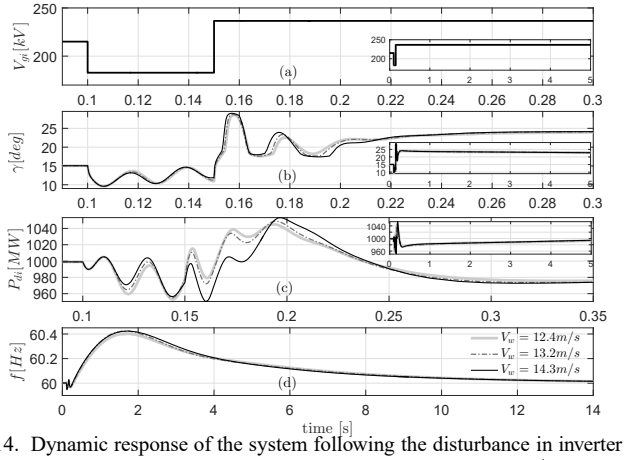

Fig. 14. Dynamic response of the system following the disturbance in inverter side grid voltage (V_{gi}). Grey trace: response with $V_w = 12.4\ m/s$; dotted trace:$V_w = 13.2\ m/s$; Black trace:$V_w = 14.3\ m/s$. (the zoomed view of V_{gi}, γ, P_{di} along with their overall view in (a), (b), and (c)).

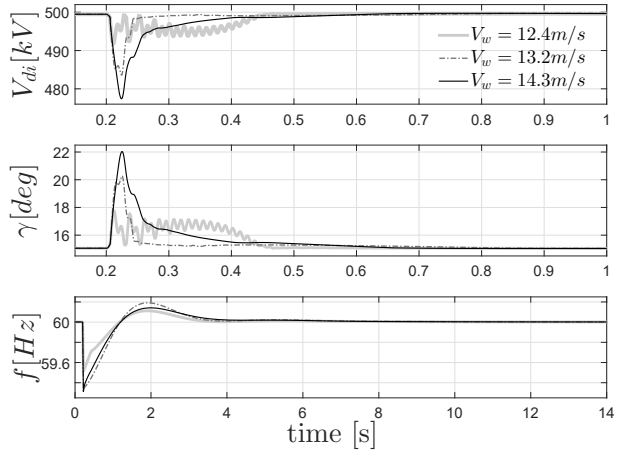

Fig. 15. Dynamic response of the system following a high impedance self-clearing fault at rectifier side AC system with $ESCR = 0.52$. Grey trace: response with $V_w = 12.4\ m/s$; dotted trace: $V_w = 13.2\ m/s$; Black trace:$V_w = 14.3\ m/s$.

VIII. Conclusion

A comprehensive modeling and small-signal stability analysis framework is developed for a DFIG-based wind farm interfacing an LCC-HVDC station in a weak AC grid where the HVDC rectifier operates in a frequency control mode. Participation factor and eigenvalue sensitivity measures indicate that the AC system electromechanical mode and the 'HVDC-PLL' mode are highly sensitive to changes in Effective DC Inertia Constant and Effective Short Circuit Ratio, respectively, which is verified through root-locus analysis in a progressively weak grid. A systematic design process of the frequency controller parameters reveals a negative interaction between the 'generator speed-HVDC PLL-frequency controller' mode and the 'DFIG-GSC controller' mode. The designed frequency controller operation was tested under different operating points after including the pitch angle control in the WF model, which further validates the robustness of the control design.

Appendix I

□ The state-equations of generator and turbine mechanical-side:

$$\begin{aligned}
\dot{\omega}_{r_dfg} &= \tfrac{1}{2H_g}\{(-C_{sh}\omega_{el}\omega_{r_dfg} + K_{sh}\theta_{tw} + C_{sh}\omega_{el}\omega_t) \\
&\quad - (\tfrac{e'_{qs}i_{qs}+e'_{ds}i_{ds}}{\omega})\} \\
\dot{\omega}_t &= \tfrac{1}{2H_t}\{(-C_{sh}\omega_{el}\omega_{r_dfg} - K_{sh}\theta_{tw} + C_{sh}\omega_{el}\omega_t) \\
&\quad + T_m\left(R, \rho, V_w, \omega_{r_dfg}\right)\} \\
\dot{\theta}_{tw} &= \omega_{el}\left(\omega_t - \omega_{r_dfg}\right)
\end{aligned} \tag{12}$$

□ The induction machine and the RSC dynamics can be modeled as follows (q-axis aligned with stator flux):

$$\begin{aligned}
\dot{i}_{qs} &= \left(\tfrac{R_r+K_{pr}}{\sigma L_{rr}} - \tfrac{\omega_{el}R_s}{L_{ss}}\right) i_{qs} + \{\tfrac{K_{pr}}{\sigma L_{rr}} - \tfrac{L_m}{L_{ss}}\left(\tfrac{R_r+K_{pr}}{\sigma L_{rr}}\right)\} i_{ms} \\
&\quad + \tfrac{L_m}{L_{ss}}\tfrac{K_{pr}}{\sigma L_r} K_{vc}\left(|v_s| - |v_s^*|\right) - \tfrac{L_m}{L_{ss}}\tfrac{K_{ir}}{\sigma L_{rr}} x_{rr1} - \tfrac{\omega_{el}}{L_{ss}} v_{qs} \\
\dot{i}_{ds} &= \left(\tfrac{R_r+K_{pr}}{\sigma L_{rr}}\right) i_{ds} - \tfrac{L_m}{L_{ss}}\tfrac{K_{ir}}{\sigma L_{rr}} x_{rr2} - \tfrac{K_{opt}}{L_m}\tfrac{K_{pr}}{\sigma L_{rr}}\tfrac{1}{i_{ms}}\omega^2_{r_dfg} \\
\dot{e}'_{qs} &= \tfrac{\omega_{el}\omega}{\left(\frac{L_{fr}K^2_{mrr}}{aL'_s}+1\right)}\{-\tfrac{K^2_{mrr}}{a} L_{fr}\omega_{r_dfg} i_{qs} - \tfrac{e'_{qs}}{aT_r\omega} \\
&\quad + \left(R_2 - \tfrac{L_{fr}K^2_{mrr}R_s}{aL'_s}\right) i_{ds} + \left(\tfrac{L_{fr}K^2_{mrr}}{aL'_s} + s_l\right) e'_{ds} \\
&\quad - \tfrac{L_{fr}K^2_{mrr}}{aL'_s} v_{ds} - \tfrac{K_{mrr}}{a} v_{dt}\} \\
\dot{e}'_{ds} &= \tfrac{\omega_{el}\omega}{\left(\frac{L_{fr}K^2_{mrr}}{aL'_s}+1\right)}\{-\tfrac{K^2_{mrr}}{a} L_{fr}\omega_{r_dfg} i_{ds} - \tfrac{e'_{ds}}{aT_r\omega} \\
&\quad - \left(R_2 - \tfrac{L_{fr}K^2_{mrr}R_s}{aL'_s}\right) i_{qs} - \left(\tfrac{L_{fr}K^2_{mrr}}{aL'_s} + s_l\right) e'_{qs} \\
&\quad + \tfrac{L_{fr}K^2_{mrr}}{aL'_s} v_{qs} + \tfrac{K_{mrr}}{a} v_{qt}\} \\
\dot{i}_{ms} &= -\left(\tfrac{\omega_{el}}{L_m}\right)\left(R_s i_{qs} + v_{qs}\right)
\end{aligned} \tag{13}$$

where,

$$\begin{aligned}
v_{dt} &= K_{ir}x_{rr2} + K_{pr}\left(\tfrac{L_{ss}K_{opt}\omega^2_{r_dfg}}{L^2_m i_{ms}} - i_{dr}\right) \\
&\quad - s_l\omega\{(\sigma L_{rr} + L_{fr})\, i_{qr} + \tfrac{L^2_m}{L_{ss}} i_{ms}\} \\
v_{qt} &= K_{ir}x_{rr1} + K_{pr}\{i_{ms} + K_{vc}\left(|v_s^*| - |v_s|\right) - i_{qr}\} \\
&\quad + s_l\omega\left(\sigma L_{rr} + L_{fr}\right) i_{dr}
\end{aligned}$$

$$\begin{aligned}
L_{ss} &= L_s + L_m, & L_{rr} &= L_r + L_m \\
K_{mrr} &= L_m/L_{rr}, & L'_s &= L_{ss} - L_m/K_{mrr} \\
\sigma &= 1 - L^2_m/(L_{ss}L_{rr}), & a &= 1 + (L_{fr}/L_{rr}) \\
R_2 &= K^2_{mrr}(R_{fr} + R_r), & T_r &= L_{rr}/(R_{fr} + R_r) \\
i_{dr} &= -\tfrac{L_{ss}}{L_m} i_{ds}, & i_{qr} &= i_{ms} - \tfrac{L_{ss}}{L_m} i_{qs} \\
K_{opt} &= 0.5\rho\pi R^5 C_{Popt}/\lambda^3_{opt}
\end{aligned}$$

Copyright (c) 2017 IEEE. Personal use is permitted. For any other purposes, permission must be obtained from the IEEE by emailing pubs-permissions@ieee.org.

This is the author's version of an article that has been published in this journal. Changes were made to this version by the publisher prior to publication.
The final version of record is available at http://dx.doi.org/10.1109/TPWRD.2016.2607205

□ The DC link and the GSC (q-axis aligned with v_s) shown in Fig. 2 can be modeled as described below:

$$\dot{v}_{dc}^2 = -\frac{3}{C}\left[v_{dt}i_{dr} + v_{qt}i_{qr} + v_{dg}i_{dg} + v_{qg}i_{qg}\right] \tag{14}$$

$$\begin{aligned}
\dot{i}_{qg} &= -\left(\frac{R_{fg}+K_{pg}}{L_{fg}}\right)i_{qg} + \left(\frac{K_{ig}}{L_{fg}}\right)x_{g1} + \left(\frac{K_{pg}}{L_{fg}}\right)i_{qg}^* \\
\dot{i}_{dg} &= -\left(\frac{R_{fg}+K_{pg}}{L_{fg}}\right)i_{dg} + \left(\frac{K_{ig}}{L_{fg}}\right)x_{g2} - \left(\frac{K_{pg}}{L_{fg}}\right)\left(\frac{2Q_{gsc}^*}{3v_{qs}}\right)
\end{aligned} \tag{15}$$

Note that v_{qg} and v_{dg} can be expressed as:

$$\begin{aligned}
v_{qg} &= K_{ig}x_{g2} + K_{pg}\left(i_{qg}^* - i_{qg}\right) - \omega L_{fg}i_{dg} + v_{qs} \\
v_{dg} &= K_{ig}x_{g1} + K_{pg}\left(-\frac{2Q_{gsc}^*}{3v_{qs}} - i_{dg}\right) + \omega L_{fg}i_{qg} + v_{ds}
\end{aligned} \tag{16}$$

□ The state equations of the RSC and the GSC current control loops (Fig. 2) are shown in equation (17).

$$\begin{aligned}
\dot{x}_{rr1} &= i_{ms} + K_{vc}\left(|V_s^*| - |v_s|\right) - i_{qr} \\
\dot{x}_{rr2} &= \left(\frac{L_{ss}K_{opt}}{L_m^2 i_{ms}}\omega_{r_dfg}^2 - i_{dr}\right) \\
\dot{x}_{g1} &= \left(i_{qg}^* - i_{qg}\right) \\
\dot{x}_{g2} &= \left(-\frac{2Q_{gsc}^*}{3v_{qs}} - i_{dg}\right)
\end{aligned} \tag{17}$$

APPENDIX II

A. DFIG parameters (p.u) on 1.667 MVA, 575 kV base:

$L_s = 0.1714$, $R_s = 0.00706$, $L_m = 2.904$, $L_r = 0.1563$
$R_r = 0.005$, $C = 0.7477$, $H_t = 3.5s$ $H_g = 4.55\ s$
$L_{fr} = 4.752$, $R_{fr} = 0.0761$, $L_{fg} = 2.311$, $R_{fg} = 0.0338$
$C_{sh} = 0.09$ pu.s/elect.rad, $K_{sh} = 0.3$ pu/elect.rad, $\lambda_{opt} = 10.5$

B. LCC-HVDC parameters:

$B_i = 2$, $B_r = 2$, $R_{dc} = 5\ \Omega$,
$C_{dc} = 26\ \mu F$, $X_{ci} = 13.2062\ \Omega$, $X_{cr} = 13.0956\ \Omega$
$L_{dc} = 1.1936\ H$, $tap_i = 1$, $tap_r = 1$

C. AC grid (dynamic model) parameters (p.u) on 900 MVA, 20 kV base [3]:

$X_d = 1.8$, $X_q = 1.7$, $X_l = 0.2$, $X'_d = 0.3$
$X'_q = 0.55$, $X''_d = 0.25$, $X''_q = 0.25$, $R_a = 0.0025$
$T'_{d0} = 8.0\ s$, $T'_{q0} = 0.4\ s$, $T''_{d0} = 0.03\ s$, $T''_{q0} = 0.05\ s$

D. State-space averaged model variables:

The following are the state variables, input variables, and the algebraic variables obtained when the state-space model is linearized around the operating point (refer Table II).

State variables, x_0:

$\hat{\theta}_2 = 0.046\ pu$, $x_{rr1} = -0.020$, $x_{pll(2)} = 0$, $i_{qs} = 8.340\ pu$
$i_{ds} = 4.532\ pu$, $x_{rr2} = 0.045$, $x_{rf} = 0$, $i_{ms} = 3.962\ pu$,
$v_{dc}^2 = 5.928\ pu$, $i_{qg} = 0.951\ pu$, $i_{dg} = 0$, $\theta_{tw} = 2.683\ rad$.
$\omega_t = 1.180\ pu$, $x_{g1} = 0.005$, $x_{g2} = 0$, $\omega_{r-dfg} = 1.18\ pu$
$e'_{qs} = 0.908\ pu$, $x_{i1} = 0.036$, $I_{dr} = 2\ A$, $i_{qg}^* = 0.951\ pu$
$e'_{ds} = 0.292\ pu$, $x_{r1} = 0.030$, $I_{di} = 2\ A$, $v_{dm} = 504.5\ kV$

Input variables, u_0:

$I_d^* = 2\ A$, $|v_s^*| = 0.817\ pu$, $V_w = 13.2\ m/s$, $\theta_2 = 0.046\ pu$,
$Q_{gsc}^* = 0$, $(v_{dc}^*)^2 = 5.928\ pu$, $\gamma_i^* = 0.263\ rad$.

Algebraic variables, z_0:

$|v_s| = 1.035\ pu$, $v_{qs} = 1.035\ pu$, $E_{acr} = 367.0\ kV$,
$E_{aci} = 231.8\ kV$, $\alpha_{r0} = 367.0\ kV$

E. Pitch angle control:

The parameters of the pitch angle controller (Fig. 16) are:
$K_{pp} = 1\ deg$, $K_{ip} = 40\ deg.s^{-1}$

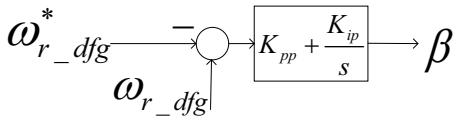

Fig. 16. Schematic of the pitch angle (β) controller [16].

REFERENCES

[1] U.S. Department of Energy, Tech. Rep. May 2008. "20% wind energy by 2030: Increasing wind energy's contribution to U.S. electricity supply".
[2] Midwest ISO, PJM, SPP and TVA, Tech. Rep., 2008. "Joint coordinated system plan 2008," Available: http://www.jcspstudy.org/.
[3] P. Kundur, *Power system stability and control*, ser. The EPRI power system engineering series. New York; London: McGraw-Hill, 1994.
[4] "Guide for planning DC links terminating at AC locations having low short-circuit capacities, part i: AC/DC interaction phenomena," *CIGRE' and IEEE Joint Task Force Report, CIGRE' Publication*, vol. 68, Jun 1992.
[5] L. Wang and K. H. Wang, "Dynamic stability analysis of a DFIG-based offshore wind farm connected to a power grid through an HVDC link," *IEEE Transactions on Power Systems*, vol. 26, no. 3, pp. 1501–1510, Aug 2011.
[6] D. Xiang, L. Ran, J. Bumby, P. Tavner, and S. Yang, "Coordinated control of an HVDC link and doubly fed induction generators in a large offshore wind farm," *IEEE Transactions on Power Delivery*, vol. 21, no. 1, pp. 463–471, Jan 2006.
[7] H. Yin, L. Fan, and Z. Miao, "Coordination between DFIG-based wind farm and LCC-HVDC transmission considering limiting factors," in *Energytech, 2011 IEEE*, May 2011, pp. 1–6.
[8] H. Yin and L. Fan, "Modeling and control of DFIG-based large offshore wind farm with HVDC-link integration," in *North American Power Symposium (NAPS)*, Oct 2009, pp. 1–5.
[9] S. V. Bozhko, R. Blasco-Gimenez, R. Li, J. C. Clare, and G. M. Asher, "Control of offshore DFIG-based wind farm grid with line-commutated HVDC connection," *IEEE Transactions on Energy Conversion*, vol. 22, no. 1, pp. 71–78, March 2007.
[10] S. Bozhko, G. Asher, R. Li, J. Clare, and L. Yao, "Large offshore DFIG-based wind farm with line-commutated HVDC connection to the main grid: Engineering studies," *IEEE Transactions on Energy Conversion*, vol. 23, no. 1, pp. 119–127, March 2008.
[11] H. Zhou and G. Yang, "Control of DFIG-based wind farms with hybrid HVDC connection," in *IEEE 6th International Power Electronics and Motion Control Conference,IPEMC.*, May 2009, pp. 1085–1091.
[12] H. Zhou, G. Yang, and J. Wang, "Modeling, analysis, and control for the rectifier of hybrid HVdc systems for DFIG-based wind farms," *IEEE Trans. on Energy Conversion*, vol. 26, no. 1, pp. 340–353, March 2011.
[13] L. Ran, D. Xiang, L. Hu, and K. Abbott, "Voltage stability of an HVDC system for a large offshore wind farm with dfigs," in *The 8th IEE International Conference on AC and DC Power Transmission, ACDC*, March 2006, pp. 150–154.
[14] R. Li, S. Bozhko, and G. Asher, "Frequency control design for offshore wind farm grid with LCC-HVDC link connection," *IEEE Transactions on Power Electronics*, vol. 23, no. 3, pp. 1085–1092, May 2008.
[15] R. Pena, J. C. Clare, and G. M. Asher, "A doubly fed induction generator using back-to-back PWM converters supplying an isolated load from a variable-speed wind turbine," *IEE Proceedings on Electric Power Applications*, vol. 143, no. 5, pp. 380–387, 1996.
[16] F. Lingling, M. Zhixin, and D. Osborn, "Wind farms with HVDC delivery in load frequency control," *IEEE Transactions on Power Systems*, vol. 24, no. 4, pp. 1894–1895, 2009.
[17] Z. Miao, L. Fan, D. Osborn, and S. Yuvarajan, "Wind farms with HVdc delivery in inertial response and primary frequency control," *IEEE Trans. on Energy Conversion*, vol. 25, no. 4, pp. 1171–1178, Dec 2010.
[18] M. Zhang, X. Yuan, J. Hu, S. Wang, S. Ma, Q. He, and J. Yi, "Wind power transmission through LCC-HVDC with wind turbine inertial and primary frequency supports," in *IEEE Power Energy Society General Meeting*, July 2015, pp. 1–5.
[19] H. Yin, L. Fan, and Z. Miao, "Fast power routing through HVDC," *IEEE Transactions on Power Delivery*, vol. 27, no. 3, pp. 1432–1441, July 2012.
[20] PSCAD/EMTDC v. 4.2.1, Manitoba HVDC Research Centre, Winnipeg, MB, Canada.
[21] R. Pena, J. C. Clare, and G. M. Asher, "Doubly fed induction generator using back-to-back PWM converters and its application to variable-

Copyright (c) 2017 IEEE. Personal use is permitted. For any other purposes, permission must be obtained from the IEEE by emailing pubs-permissions@ieee.org.

This is the author's version of an article that has been published in this journal. Changes were made to this version by the publisher prior to publication.
The final version of record is available at http://dx.doi.org/10.1109/TPWRD.2016.2607205

speed wind-energy generation," *IEE Proceedings on Electric Power Applications*, vol. 143, no. 3, pp. 231–241, 1996.
[22] C. Se-Kyo, "A phase tracking system for three phase utility interface inverters," *IEEE Transactions on Power Electronics*, vol. 15, no. 3, pp. 431–438, 2000.
[23] J. E. Condren and T. W. Gedra, "Eigenvalue and eigenvector sensitivities applied to power system steady-state operating point," *Proceedings of the 45th Midwest Symposium on Circuits and Systems*, 2002.

Amirthagunaraj Yogarathinam (S'12) received his B.E. degree in Electrical and Electronic Engineering from University of Peradeniya, Sri Lanka in 2013. He is currently pursuing the Ph.D. degree at The Pennsylvania State University, PA, USA. His research interests include power system dynamics and control, HVDC, wind power integration to the modern grid, wide-area monitoring and control, application of power electronics in power systems, online system identification, nonlinear system and control, and smart grid.

Jagdeep Kaur (S'15) received her M.Tech degree in Power Electronics, Electrical Machines & Drives from Indian Institute of Technology (IIT) Delhi, India in 2013. She is currently pursuing her Ph.D. in the Pennsylvania State University, USA. Her research interests include power electronics, electrical machine drives, HVDC, renewable energy, smart grids, model reduction, and application of power electronics in power systems.

Nilanjan Ray Chaudhuri (S'08-M'09-SM'16) received his Ph.D. degree from Imperial College London, London, UK in 2011 in Power Systems. From 2005-2007, he worked in General Electric (GE) John F. Welch Technology Center. He came back to GE and worked in GE Global Research Center, NY, USA as a Lead Engineer during 2011-2014. Presently, he is an Assistant Professor with the School of Electrical Engineering and Computer Science at Penn State, University Park, PA. He was an Assistant Professor with North Dakota State University, Fargo, ND, USA during 2014-2016. He is a member of the *IEEE* and *IEEE PES*. Dr. Ray Chaudhuri is the lead author of the book *Multi-terminal Direct Current Grids: Modeling, Analysis, and Control* (Wiley/IEEE Press, 2014), and an Associate Editor of the IEEE TRANSACTIONS ON POWER DELIVERY. Dr. Ray Chaudhuri is the recipient of the National Science Foundation Early Faculty CAREER Award in 2016.

Copyright (c) 2017 IEEE. Personal use is permitted. For any other purposes, permission must be obtained from the IEEE by emailing pubs-permissions@ieee.org.